Fabrication of B doped g-C_3N_4/TiO_2 heterojunction for efficient photoelectrochemical water oxidation

Weiqian Kong[a], Xiaofan Zhang[a*], Binbin Chang[a], Yannan Zhou[a], Shouren Zhang[a], Guangli He[a], Baocheng Yang[a] and Junjie Li[b]

[a] Henan Provincial Key Laboratory of Nanocomposite and Applications, Institute of Nanostructured Functional Materials, Huanghe Science and Technology College, Zhengzhou, Henan, 450006, China.

[b] Research Technologies, Indiana University, 535 West Michigan Street, Indianapolis 46202, USA

[*]Corresponding authors.

E-mail addresses: xiaofanzhang@infm.hhstu.edu.cn

ABSTRACT: With the development of clean and renewable energy, hydrogen produced via photoelectrochemical (PEC) water splitting has attracted considerable attention. However, to develop the photoanodes with stable and excellent PEC ability is still a big challenge. In our work, TiO_2 nanorods decorated with boron doped g-C_3N_4 (BCN/TiO_2) is fabricated via thermal polymerization method to improve the PEC performance. The BCN/TiO_2 displays 4-fold increase of the photocurrent density (1.01 mA cm^{-2}) at 1.23 V vs. RHE under irradiation (100 mW cm^{-2}, AM 1.5 G). And the onset potential of BCN/TiO_2 exhibits a negative shift with 100 mV. Attributed to the broad light absorption of BCN and hetero-junction forming between BCN and TiO_2, the IPCE values are increased to 87.8% in 380 nm, and the charge separation

This is the author's manuscript of the article published in final edited form as:
Kong, W., Zhang, X., Chang, B., Zhou, Y., Zhang, S., He, G., … Li, J. (n.d.). Fabrication of B doped g-C3N4/TiO2 heterojunction for efficient photoelectrochemical water oxidation. Electrochimica Acta. https://doi.org/10.1016/j.electacta.2018.06.090

and transfer efficiency are both increased. Doping metal-free inorganic material with heteroatoms is a simple and efficient strategy to increase the light absorption within visible light and charge transfer efficiency in PEC and photocatalytic applications.

Keywords: Hetero-junction, B doped g-C_3N_4, TiO_2 Nanorods, Photoelectrochemical, Water oxidation

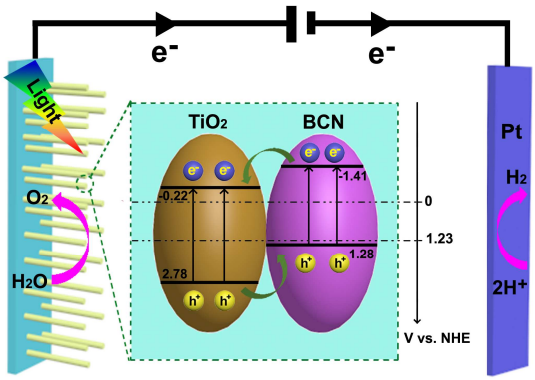

1. Introduction

Photoelectrochemical (PEC) water splitting is a promising strategy to obtain hydrogen which is the cleanest energy because of its recyclability, environmental friendliness and high energy conversion efficiency [1-4]. The solar-to-hydrogen (STH) efficiency is related to the light absorption, the separation of photo-generated charge carries and kinetics of surface reaction [5]. TiO_2 is one of the most attractive semiconductors as photoanode due to the low toxic and eco-friendly nature in addition to its low cost [3, 6]. However, TiO_2 can only absorb UV light (E_g=3~3.2 eV) and possess rapid electron/hole recombination and slow water oxidation kinetics [7, 8]. However, the STH efficiency of the TiO_2 is still very low. Until now, numerous methods have been developed to solve these problems. The various nanostructure TiO_2 have been investigated [9, 10], out of which the 1D TiO_2 nanorods (NRs) has attracted more attention as it exhibits more activate sites and provides a direct electron transport pathway for electrons [11]. Doping with non-metallic element (C [12], N/Si [13], B [14]), noble-metal decoration [15] are studied to narrow the band gap of TiO_2. Beyond that, establishing heterojunction (TiO_2/WO_3 [16], TiO_2/In_2O_3 [17], $NiTiO_3$/TiO_2 [18]), or coupling with co-catalysts [19] are also investigated to improve the photoresponse of TiO_2 in visible region and improve the separation of photogenerated electrons.

Graphitic carbon nitride (g-C_3N_4) as a metal-free inorganic semiconductor is a promising material in PEC application, which possesses high thermal and chemical stability, relatively low band gap energy (E_g) of 2.7 eV, high valence band (1.8 eV) and conduction band positions (-0.9 eV) [20, 21]. Based on the proper band gap

between TiO_2 and g-C_3N_4, g-C_3N_4/TiO_2 heterojunction has attracted more attention in photocatalytic, photoelectrochemical and degradation applications [22-25]. However, the performance of g-C_3N_4/TiO_2 is still limited by the small specific surface area, grain boundary effects and the poor electrical conductivity of g-C_3N_4 [26, 27]. Recently, doping g-C_3N_4 with heteroatoms has been widely used in photoelectrochemical cell due to its excellent light absorption and improved electric properties [28, 29]. For example, sulfur and iodine doped g-C_3N_4 can narrow the bandgap, and even decrease the reaction over-potential in comparison to g-C_3N_4 as demonstrated by DFT calculations [30, 31]. Yan *et al.* fabricated B doped g-C_3N_4 via heating the mixture of melamine and boron oxide to photo-degradate rhodamine B and methyl orange [32]. The results demonstrated B doped g-C_3N_4 exhibited more excellent activity than that of g-C_3N_4 attributed to the extended light absorption and the defected structure induced by boron doping. Ruan *et al.* fabricated a nanojunction architecture photoanode composing B doped g-C_3N_4 nanolayer and bulk g-C_3N_4. This nanojunction overcame some limitation of g-C_3N_4 and improved the charge transfer and charge separation efficiency [33]. These reports demonstrate that B doped g-C_3N_4 exhibits great potential in enhancing PEC application via forming hetero-junction. However, B doped g-C_3N_4 decorated TiO_2 nanorods has not been investigated for PEC water oxidation.

As discussed above, we construct a hetero-junction consisting of the TiO_2 nanorods (NRs) and B doped g-C_3N_4 (BCN) via in-situ thermal polymerization method. The introduction of B doping into g-C_3N_4 can extend the light absorption and

improve the conductivity. The formed heterojunction between TiO_2 and BCN is further expected to improve the light absorption, promote the charges separation and transfer process. Therefore, the BCN/TiO_2 photoanode exhibits four times higher photocurrent density (1.01 mA cm^{-2} at 1.23 V vs. RHE) than that of the TiO_2, following with a 100 mV cathodically shifted onset potential in 1 M NaOH (pH=13.6) solution. Furthermore, the charge separation increases and the transfer efficiency increase 1.4 and 2.5 times (1.23 V vs. RHE) than that of TiO_2 photoanode. The BCN/TiO_2 shows a constant evolution H_2 with 16.1 μmol h^{-1} cm^{-2} at 1.23 V vs. RHE.

2. Experimental

2.1 Prepared of all electrodes for electrochemical water oxidation

The TiO_2 nanorods (TiO_2 NRs) were grown onto FTO substrate by a hydrothermal method according to our previous report [12]. In a typical experiment, the concentrated hydrochloric acid (HCl), deionized (DI) water and titanium isopropoxide (TTIP, Sigma-Aldrich, 97%) was prepared a homogeneous solution according to the volume ratio of 3:3:0.1. Then the precursor solution was transferred into a Teflon-lined autoclave reactor, in which a piece of FTO was placed with the conductive side facing down. The hydrothermal reaction was conducted at 150℃ for 12 hours in an oven and cooled down to room temperature naturally. The obtained film was washed with DI water and dried at 60℃. Finally, the sample was annealed at 450℃ for 2 hours and the rutile TiO_2 were obtained.

Then the BCN/TiO_2 and the contrast photoanode of g-C_3N_4 modified TiO_2 (CN/TiO_2) were prepared via in-situ immersing and annealing approach. In a typical

experiment, 1 g urea with 0.7 mL 0.1 M boracic acid and no boracic acid were separately added into 14 mL H_2O solvent to obtain a homogeneous solution. Then the prepared TiO_2 was immersed into the mixed solution and maintained for 30 min. Then taken them out and dried at 80℃. Next, the samples were heated to 550℃ with a heating rate of 5℃/min, and kept for 3 hours in tube furnace. Then the BCN/TiO_2 and CN/TiO_2 photoanodes can be obtained, respectively. Besides, the pure bulk BCN powder was also prepared for comparison. In order to maintain the B doping content in BCN consistent with BCN/TiO_2, 1 g urea and 0.7 mL of 0.1 M boracic acid were added into a crucible with a cover, then heated to 550°C with a heating rate of 5℃ /min in tube furnace and maintained at this temperature for 3 hours in the Ar atmosphere. After cooling down to room temperature, the pale yellow BCN powder was obtained.

2.2 Materials and Characterization

All the chemicals were used as received, and the solutions were made with Milli-Q water. The morphology was characterized with scanning electron microscope (SEM, FEI Quanta 250 FEG) and transmission electron microscopy (TEM, FEI/Philips Tecnai G2 20) with an accelerating voltage of 200 kV. The X-ray photoelectron spectroscopy (XPS) datas were obtained on a Thermo Scientific K-Alpha X-ray photoelectron spectrometer with a monochromatized Mg Kα X ray source (hν = 1283.3 eV). The binding energy shifts were corrected by using the C1s level at 284.8 eV as an internal standard to compensate for the surface-charging effect during data analysis. X-ray diffraction (XRD) patterns were monitored by a Bruker

D8 diffractometer using Cu Kα radiation (λ = 0.15418 nm) as an X-ray source. UV-vis spectra were recorded by U-4100 (HITACHI) spectrophotometer. The photoluminescence (PL) spectra were recorded at room temperature with F-4600 (HITACHI) luminescence spectrometer. Fourier transform infrared (FT-IR) spectra was collected on a FT-IR spectrometer (Nicolet iS5, Thermo Scientific) using a standard KBr pellet technique.

2.3 Photoelectrochemical measurements

The PEC performance data were obtained with the CHI 760E (Shanghai Chenhua, China) workstation with 1 M NaOH (pH=13.6) solution as the supporting electrolyte. In addition, a three-electrode system was used in our experiment. The prepared photoanodes were used as working electrodes, the platinum (Pt) sheet was used as counter electrode and the saturated calomel electrode (SCE) was used as reference electrode. The electrolyte was purged with high-purity Ar for 30 min to remove dissolved oxygen and carbon dioxide, which can prevent the compete reaction from oxygen reduction and the decreasing of the pH value [34]. The solution is irradiated using a 500 W Xe-lamp (CEL-500, CEAULIGHT), which is coupled with an AM 1.5 G filter. The light power density was calibrated to 100 mW cm^{-2} with light power meter (CEL-NP2000-2). Linear sweep voltammetry (LSV) was performed with a scan rate of 10 mV s^{-1}. The stability test was carried out with amperometric measurements (i-t) under illumination (100 mW cm^{-2}, AM 1.5 G), which the voltage was at a fixed potential of 1.23 V vs. RHE. The monochromatic IPCE was also calculated at a fixed potential of 1.23 V vs. RHE using different cut-off filters (365

nm, 380 nm, 420 nm, 435 nm, 450 nm, 475 nm, 500 nm and 550 nm). The electrochemical impedance spectroscopy (EIS) was documented in the frequency range of 100 kHz to 0.01 Hz with an AC voltage amplitude of 10 mV at a bias of 0.2 V vs. RHE in 1 M NaOH solution. The Mott-Schottky plot was collected in a potential range of -0.8~0.6 V vs. RHE with a frequency of 1 kHz in the dark. The evolved H_2 and O_2 were detected using gas chromatography (GC-7920, China, detection limit: H_2 50 ppm, O_2 1000 ppm) with Ar as a carrier gas. The gas evolution by photoelectrodes was regularly collected by a manual injector quantitatively analyzed by gas chromatography (GC). And the amount gases were calculated according to the corresponding standard curve, respectively. All the electrochemical experiments were carried out at room temperature. All the potential in the experiment was converted to reversible hydrogen electrode (RHE) by the Nernst equation:

$$E_{RHE} = E_{vs.SCE} + E^{\circ}_{SCE} + 0.059pH$$

where the E°_{SCE} is 0.2412 V at 25°C.

3. Results and discussion

As illustrated in Fig. 1, the TiO_2 NRs photoanodes is obtained via hydrothermal method [12] was chosen as a prototype for investigating the PEC performance. Then the TiO_2 NRs is decorated with BCN after impregnation and annealing treatment.

SEM and TEM images are characterized the morphologies and structures of the TiO_2 and BCN/TiO_2. As shown in Fig. 2a, the TiO_2 are uniformly grown onto FTO with the average diameter of 80-150 nm and a length of 3 μm (inset of Fig. 2a). The BCN islands are clearly observed on TiO_2 via a thermal polymerization route (Fig. 2b).

Fig. 2c provides the clear morphology of a single nanorod of TiO_2. The lattice fringe of 0.323 nm (inset of Fig. 2c) is corresponding to the (110) plane of tetragonal TiO_2. Fig. 2d shows the TiO_2 is all surrounded with the BCN film, which agrees well with the linear EDX image (Fig. S1). The boundary between BCN and TiO_2 can be distinctly observed in Fig. S2. The thickness of the surrounded BCN film is calculated to be 2~10 nm. To further testify the existence of BCN, the FT-IR spectra of the TiO_2, BCN, and BCN/TiO_2 are further confirmed (Fig. S3**)**. Compared to the TiO_2 NRs and BCN, the typical peaks of BCN can be clearly observed in BCN/TiO_2 at ~3200 cm^{-1} (C-H) and 1250~1650 cm^{-1} (C-N) [35]. And the characteristic peak of Ti-O is found at 500~1000 cm^{-1} [36]. These results indicate the existence of BCN in the BCN/TiO_2.

The X-ray photoelectron spectroscopy (XPS) is analyzed to determine the element analysis and chemical composition of all samples. Fig. 3 illustrates the XPS survey spectra and high-resolution XPS spectra of different elements. Fig. 3a represents the presence of B, C, O, N and Ti atoms, which is consistent with the linear EDX image. Fig. 3b has displayed the high-resolution B 1s peaks of BCN and BCN/TiO_2. The peak at 192.0 eV of the BNC is corresponding to the typical B-N bond [37, 38]. The peak at 190.7 eV of the BCN/TiO_2 is at a lower binding energy than that of BCN, indicating some of the boron atoms are less electropositive than that of BCN [37]. The characteristic peak of Ti-O-B-O-Ti (191.6 eV) is not discovered in BCN/TiO_2 [14], indicating no B atom doped into the TiO_2 nanorod lattice for BCN/TiO_2. Fig. 3c has shown the high-resolution spectra of Ti 2p in BCN and BCN/TiO_2. The Ti 2p XPS spectrum is divided by Ti $2p_{3/2}$ and Ti $2p_{1/2}$ peaks. For

pristine TiO_2, the Ti can be fitted with the binding energies of 458.8 eV and 464.6 eV peak for Ti $2p_{3/2}$ and Ti $2p_{1/2}$, respectively [39, 40]. After modified with BCN, the two Ti 2p peaks decrease to 458.6 eV and 464.4 eV, respectively. The negative shift of Ti 2p can be attributed to the changing of electron cloud density around TiO_2 surface binding interaction, which is consistent with the positive shift of B atom in BCN/TiO_2. This phenomenon predicts an electron transfer from BCN to TiO_2 [19]. As shown in Fig. 3d, the C1s XPS spectrum of BCN/TiO_2 reveals three different signals at 284.7, 286.0 and 288.7 eV, respectively. The peak at 284.8 eV is ascribed to graphitic carbon. The weaker C peak located at 288.7 eV can be assigned to sp^2-bonded carbon (N–C=N) [20]. As a result, the BCN is successfully covered onto the surface of TiO_2 photoanode, which is consistent with the results of the TEM images and FT-IR spectra.

The crystal structure is revealed by X-ray diffraction (XRD) as shown in Fig. 4a. The obvious peak of BCN spectrum at 27.5º can be indexed to the (002) interlayer spacing and correspond to the characteristic inter-planar staking peak of aromatic system [31]. The diffraction peaks at 36.4º, 62.5º and 65.8º are corresponding to the (101), (002) and (112) crystal plans of rutile TiO_2, respectively (JCPDS 21-1276) [41]. The BCN/TiO_2 shows no diffraction peaks at 27.5º, owing to a small amount of BCN. Apart from the peaks of the BCN and TiO_2, there is no additional peak can be observed in BCN/TiO_2, indicating the BCN can not change the crystal phase of TiO_2. In order to investigate the influence of BCN on the light absorption, the normalized UV-vis spectra of TiO_2, BCN and BCN/TiO_2 are collected. As Fig. 4b shown, the

spectrum of TiO_2 shows a strong absorption in UV region but decreases sharply at the wavelength of 410 nm. The slight absorption in visible region is caused by the undetected light scattering, which nearly has no effect during the PEC water splitting process [42]. The absorption edge of BCN is about 470 nm. It can be clearly observed that the BCN/TiO_2 show slightly red-shifted compared to TiO_2, which is ascribed to the light absorption of BCN [43]. According to the Tauc plot $((\alpha h\nu)^{1/2}$ vs. $h\nu$), the band gap of TiO_2, BCN and BCN/TiO_2 are calculated to be 3.0 eV, 2.69 eV and 2.9 eV, respectively [12, 44]. The changing of band gap can be attributed to the bonding between BCN and TiO_2. The result indicates an extended absorption is endowed to the BCN/TiO_2 which implies a better PEC performance. PL spectra is a convenient technology to indirectly evaluate the charge separation and transfer abilities [45, 46]. As Fig. S4 shown, the PL intensity of CN/TiO_2 is smaller than that of the TiO_2. For BCN/TiO_2, the PL intensity can be further decreased, implying the charge separation may be further promoted by BCN/TiO_2 than that of CN/TiO_2. These results demonstrate the increased light absorption and improved separation of photo-generated charge carriers will be beneficial for PEC water oxidation.

The PEC performance of all prepared photoanodes are investigated both in dark and light illumination and the results are shown in Fig. 5. The LSV curves of the TiO_2 and BCN/TiO_2 were recorded in 1 M NaOH electrolyte under light irradiation (AM 1.5 G, 100 mW cm^{-2}). Firstly, a series of BCN/TiO_2 obtained with different concentrations of BCN were tested to optimize the content of BCN. The prepared BCN/TiO_2 was denoted as x % BCN/TiO_2 according to the content of the urea

precursor (x wt%), and the results are shown in Fig. S5. Among them, the highest photocurrent density can be obtained for the BCN/TiO_2 (7 %). In the dark, the TiO_2 and BCN/TiO_2 photoanodes show negligible current over the whole potential window (Fig. 5a). For comparison, the photocurrent densities of TiO_2, CN/TiO_2 and BCN/TiO_2 are both measured under light illumination. As shown in Fig. 5a**,** the photocurrent density of the CN/TiO_2 is 2.9 times higher than that of the pristine TiO_2 (0.23 mA cm^{-2}, E_{RHE}=1.23V). After B doping, the photocurrent density of the BCN/TiO_2 further increases to 1.01 mA cm^{-2} (E_{RHE}=1.23V), which is approximate four times larger than that of TiO_2. In addition, the onset potential of the BCN/TiO_2 cathodically shifts 100 mV. The incident photo-to-current efficiency (IPCE) is measured under light illumination at 1.23 V vs. RHE with different cut-off filters, which can be calculated with the following equation:

$$\mathrm{IPCE}(\%) = \left[1240 \times J_p / \left(\lambda \times P(\lambda)\right)\right] \times 100\%$$

where J_P is the photocurrent density (mA cm^{-2}), P(λ) is the incident-light power density for each wavelength (mW cm^{-2}), and the λ is the incident-light wavelength (nm). As shown in Fig. 5b, the maximum IPCE values of TiO_2 and BCN/TiO_2 are both recorded at 380 nm, which are 36.6% and 87.8%, respectively. Furthermore, in the entire visible region investigated, the IPCE values of BCN/TiO_2 are already two times higher than that of the TiO_2 photoanode (inset of Fig. 5b). In a word, the BCN/TiO_2 shows a better IPCE response over the entire wavelength range investigated, which is well matched with the UV-vis spectra.

To investigate the charge transfer process, the EIS measurement was performed

in dark and light illumination (AM 1.5 G, 100 mW cm^{-2}) at an AC frequency from 100 kHz to 0.01 Hz. As shown in Fig. 5c, the Nyquist plot of BCN/TiO_2 obtained in dark exhibits a smaller diameter than that of the CN/TiO_2, indicating the conductivity can be improved after B doped g-C_3N_4. Under illumination, the BCN/TiO_2 displays the smallest charge transfer resistance (R_{ct}) among the TiO_2, CN/TiO_2 and BCN/TiO_2 photoanodes, indicating the charge transfer process can be promoted at the interfacial of photoanode/electrolyte. The result indicates the charge-transfer barrier at the electrode interface is decreased, so that the water oxidation reaction is easier to occur and a cathodically shift of onset potential appears [47]. These results agree well with the LSV curves (Fig. 5a) and PL spectra (Fig. S4). In order to deeply investigate the intrinsic electronic properties, Mott-Schottky (MS) plots are collected in dark to obtain the flat-band potential (E_{fb}). Just as Fig. 5d and Fig. S6 shown, the positive slopes of TiO_2 and BCN plots indicate the n-type semiconductor of TiO_2 and BCN. And the flat-band potential (E_{fb}) of TiO_2, CN/TiO_2 and BCN/TiO_2 is calculated to be -0.06 V, -0.12 V and -0.23 V vs. RHE, respectively. The negative shift of E_{fb} implies the charge flow from BCN to TiO_2, which decreases the chance of electron/hole recombination [24]. Simultaneously, the MS result demonstrates the BCN/TiO_2 has the highest charge transfer efficiency compared with TiO_2 and CN/TiO_2, which is conductive to improve PEC water oxidation performance.

For further investigating the PEC performance of BCN/TiO_2, the light harvesting efficiency (LHE, LHE=1-10^{-A}), charge separation efficiency (η_{sep}) and surface charge transfer efficiency ($\eta_{transfer}$) are calculated. Fig. 6a shows the LHE spectra of the TiO_2

and BCN/TiO_2. It is obvious that the LHE enhancement of the BCN/TiO_2 (1.1 times) is much smaller than the IPCE enhancement (2.4 times), which indicates the extended light absorption is not the main reason for the enhanced PEC performance. In order to explore the detail information of charge separation efficiency and surface charge transfer efficiency, a hole scavenger (Na_2SO_3) was added into the electrolyte during the experiment, which can eliminate the energy loss in the oxidation process [48]. Fig. S7 displays the LSV curves of TiO_2 and BCN/TiO_2 before and after adding 0.1 M Na_2SO_3. Since the hole capture kinetics of Na_2SO_3 at the semiconductor/electrolyte surface is very fast, the charge injection efficiency can be assumed 100% [49]. The photocurrent density of PEC water oxidation can be described by $J_{H2O}=J_{abs}\times\eta_{sep}\times\eta_{transfer}$ without 0.1 M Na_2SO_3. Thus, the photocurrent density after adding Na_2SO_3 can be calculated by $J_{H2O}=J_{abs}\times\eta_{sep}$. According to our previous report [50], the J_{abs} of the TiO_2 and BCN/TiO_2 photoanodes are calculated to be 1.6 $mA\cdot cm^{-2}$ and 2.0 $mA\cdot cm^{-2}$ (Fig. 6b), respectively. The addition of Na_2SO_3 has no effect in changing the pH, light absorption or E_{fb} for the electrodes, so the J_{abs} should be same for each photoanodes. Thus, the η_{sep} and $\eta_{transfer}$ can be obtained by J_{Na2SO3}/J_{abs} and J_{H2O}/J_{Na2SO3}, respectively. Fig. 6c expresses that the charge separation efficiency of the BCN/TiO_2 is higher (54.9%, vs. 1.23 V) th an that of pristine TiO_2 (38.9%, vs. 1.23 V). This implies the recombination of photo-generated electron/hole pairs is effectively restrained after modified with BCN, owing to the efficient improved charge transfer from BCN to TiO_2. As exhibited in Fig. 6d, the prominent enhanced charge transfer efficiency is observed in BCN/TiO_2 photoanode (91%, vs. 1.23 V), which increases

1.53 times than that of TiO_2 photoanode (36%, vs. 1.23 V). Therefore, the BCN/TiO_2 composite photoanode has excellent photocatalytic activity on PEC water splitting.

The stable performance of the TiO_2 and BCN/TiO_2 electrodes for water oxidation is also investigated. The stabilities are evaluated with amperometric measurements (i-t) under illumination (100 mW cm^{-2}, AM 1.5 G), which the potential is set at 1.23 V (vs. RHE). Fig. 7a has displayed the corresponding i-t curves of BCN/TiO_2 and TiO_2 photoanodes. For BCN/TiO_2 photoanode, the photocurrent density goes steadily with the time increasing and has no obvious decay even after 6 h. On the contrary, the TiO_2 electrode exhibits reduced stability, which the photocurrent density decreases approximately 19% after 6 h. This result indicates that BCN could be contributed to the augmented stability of TiO_2 electrode.

In order to validate whether the anodic photocurrent generated by the photoanode is the exclusive result of O_2 evolution, the produced H_2 and O_2 are both quantified by GC under light irradiation (AM 1.5 G, 100 mW cm^{-2}). In addition, the gas products are injected into gas chromatography (GC) for quantitative analysis. As Fig. 7b shown, the constant H_2 evolution of BCN/TiO_2 photoanode is ~16.1 μmol h^{-1} cm^{-2} with the testing period of 6 h, which is 10.7 times larger than that of pristine TiO_2 photoanode (1.5 μmol h^{-1} cm^{-2}). The O_2 evolution of BCN/TiO_2 is about 7.4 μmol h^{-1} cm^{-2}. In addition, the molar ratio of the produced H_2 and O_2 is 2.17, which is close to the theoretical value for overall water splitting. As a consequence, the introduction of BCN indeed enhances the PEC water splitting process.

The mechanism of the BCN/TiO_2 photoanode for enhanced PEC performance is

also been proposed (Fig. 8). The valence band (VB) of BCN is calculated to be 5.72 eV by subtracting the secondary electron onset position of the He I UPS spectra from the excitation energy (21.2 eV) (Fig. S8) [51]. The valence band of TiO_2 is 7.22 eV as reported by our previous study [52]. The bandgap of TiO_2 and BCN are determined to be 3.0 eV and 2.69 eV from Tauc plots (Inset of Fig. 4b). Therefore, the conduction band (CB) of the TiO_2 and BCN is calculated to be 4.22 eV and 3.03 eV, respectively. According to the reference standard for which 0 V versus RHE equals -4.44 eV versus evac (vacuum level), the VB and CB values of TiO_2 and BCN in electron volts can be converted to electrochemical energy potentials in volts. Consequently, the VB values of TiO_2 and BCN are 2.78 and 1.28 V (vs. RHE), respectively. Obviously, the CB values for TiO_2 and BCN is -0.22 and -1.41 V (vs. RHE). Based on the matching band gap positions, a heterojunction is formed between the BCN and TiO_2, which is the driving force of charge transfer [53]. Under light illumination, BCN and TiO_2 absorb incident light and generate the electron-hole pairs. Attributed to the appropriate position and the build-in electric field, the photo-generated holes can transfer from TiO_2 to BCN, and electrons transfer in the opposite direction. Finally, the holes captured water molecular for O_2 evolution in the interface of photoanode/electrolyte, and the electrons are consumed by H^+ for H_2 generation at the Pt counter electrode. Consequently, the BCN/TiO_2 increases the PEC water splitting.

4. Conclusions

In summary, the BCN/TiO_2 photoanode was successfully synthesized by a facile

thermal polymerization method. As results, the BCN/TiO_2 displays 4-fold increase of the photocurrent density (1.01 mA cm^{-2}) at 1.23 V vs. RHE under irradiation (AM 1.5 G, 100 mW cm^{-2}). And the onset potential of BCN/TiO_2 exhibits a negative shift with 100 mV. Attributed to the heterojunction between BCN and TiO_2, the charge separation and transfer efficiencies of the BCN/TiO_2 display a remarkable enhancement, which are 1.4 and 2.5 times (1.23 V vs. RHE) than that of TiO_2 photoanode, respectively. The maximum IPCE value is increased to 87.8% in 380 nm. Besides, the IPCE value approximately two times higher than that of TiO_2 in the entire visible region investigated. The constant H_2 evolution of BCN/TiO_2 is approximately 16.1 μmol h^{-1} cm^{-2} at 1.23 V (vs. RHE). The observation of this study provides rational strategies for designing composite photoelectrodes by tuning compositions and forming heterojunction to enhance PEC water splitting efficiency.

Acknowledgements

This work is supported by the National Natural Science Foundation of China (51602120, 51702114), Natural Science Foundation of Education Department of Henan Province (17A430023, 18A150011).

References

[1] M. Walter, E. Warren, J. Mckone, S. Boettcher, Q. Mi, E. Santori, N. Lewis, Solar water splitting cells, Chem. Rev. 110 (2010) 6446-6473.

[2] C. Jiang, S. Moniz, A. Wang, T. Zhang, J. Tang, Photoelectrochemical devices for solar water splitting-materials and challenges, Chem. Soc. Rev. 46 (2017)

4645-4660.

[3] A. Fujishima, K. Honda, Electrochemical photolysis of water at a semiconductor electrode, Nature 237 (1972) 37-38.

[4] P. Yilmaz, A. Lacerda, L. Larrosa, S. Dunn, Photoelectrocatalysis of Rhodamine B and solar hydrogen production by TiO_2 and Pd/TiO_2 Catalyst Systems, Electrochim. Acta 231 (2017) 641-649.

[5] H. Dotan, K. Sivula, M. Gratzel, A. Rothschild, S. Warren, Probing the photoelectrochemical properties of hematite (α-Fe_2O_3) electrodes using hydrogen peroxide as a hole scavenger, Energy Environ. Sci. 4 (2011) 958-964.

[6] X. Chen, S. Shen, L. Guo, S. Mao, Semiconductor-based photocatalytic hydrogen generation, Chem. Rev. 110 (2010) 6503-6570.

[7] E. Hendry, M. Koeberg, B. O'Regan, M. Bonn, Local field effects on electron transport in nanostructured TiO_2 revealed by terahertz spectroscopy, Nano Lett. 6 (2006) 755-759.

[8] Y. Nah, I. Paramasivam, P. Schmuki, Doped TiO_2 and TiO_2 nanotubes: synthesis and applications, Chem. Phys. Chem. 11 (2010) 2698-2713.

[9] Y. Tang, P. Wee, Y. Lai, X. Wang, D. Gong, P. Kanhere, T. Lim, Z. Dong, Z. Chen, Hierarchical TiO_2 nanoflakes and nanoparticles hybrid structure for improved photocatalytic activity, J. Phys. Chem. C 116 (2012) 2772-2780.

[10] B. Aragaw, C. Pan, W. Su, H. Chen, J. Rick, B. Hwang, Facile one-pot controlled synthesis of Sn and C codoped single crystal TiO_2 nanowire arrays for highly efficient photoelectrochemical water splitting, Appl. Catal. B 163 (2015)

478-486.

[11] T. Fröschl, U. Hörmann, P. Kubiak, G. Kučerová, M. Pfanzelt, C.K. Weiss, R.J. Behm, N. Hüsing, U. Kaiser, K. Landfester, M. Wohlfahrt-Mehrens, High surface area crystalline titanium dioxide: potential and limits in electrochemical energy storage and catalysis, Chem. Soc. Rev. 41 (2012) 5313-5360.

[12] X. Zhang, B. Zhang, Z. Zuo, M. Wang, Y. Shen, N/Si co-doped oriented single crystalline rutile TiO_2 nanorods for photoelectrochemical water splitting, J. Mater. Chem. A 3 (2015) 10020-10025.

[13] N. Lu, X. Quan, J. Li, S. Chen, H. Yu, G. Chen, Fabrication of boron-doped TiO_2 nanotube array electrode and investigation of its photoelectrochemical capability, J. Phys. Chem. C 111 (2007) 11836-11842.

[14] G. Bessegato, J. Cardoso, M. Zanoni, Enhanced photoelectrocatalytic degradation of an acid dye with boron-doped TiO2 nanotube anodes, Catal. Today 240 (2015) 100-106.

[15] X. Zhang, Y. Liu, S. Lee, S. Yang, Z. Kang, Coupling surface plasmon resonance of gold nanoparticles with slow-photon-effect of TiO_2 photonic crystals for synergistically enhanced photoelectrochemical water splitting, Energy Environ. Sci. 7 (2014) 1409-1419.

[16] T. Tatsuma, S. Saitoh, Y. Ohko, A. Fujishima, TiO_2-WO_3 Photoelectrochemical anticorrosion system with an energy storage ability, Chem. Mater. 13 (2001) 2838-2842.

[17] Z. Jiang, D. Jiang, Z. Yan, D. Liu, K. Qian, J. Xie, A new visible light active

multifunctional ternary composite based on TiO_2-In_2O_3 nanocrystals heterojunction decorated porous graphitic carbon nitride for photocatalytic treatment of hazardous pollutant and H_2 evolution, Appl. Catal. B 170 (2015) 195-205.

[18] S. Moghiminia, H. Farsi, H. Raissi, Comparative optical and electrochemical studies of nanostructured $NiTiO_3$ and $NiTiO_3$-TiO_2 prepared by a low temperature modified sol-gel route, Electrochim. Acta 132 (2014) 512-523.

[19] F. Ning, M. Shao, S. Xu, Y. Fu, R. Zhang, M. Wei, D. Evans, X. Duan, TiO_2/graphene/NiFe-layered double hydroxide nanorod array photoanodes for efficient photoelectrochemical water splitting, Energy Environ. Sci. 9 (2016) 2633-2643.

[20] J. Liu, Y. Liu, N. Liu, Y. Han, X. Zhang, H. Huang, Y. Lifshitz, S. Lee, J. Zhong, Z. Kang, Metal-free efficient photocatalyst for stable visible water splitting via a two-electron pathway, Science 347 (2015) 970-974.

[21] X. Wang, K. Maeda, A. Thomas, K. Takanabe, G. Xin, J. Carlsson, K. Domen, M. Antonietti, A metal-free polymeric photocatalyst for hydrogen production from water under visible light, Nat. Mater. 8 (2009) 76-80.

[22] Y. Li, R. Wang, H. Li, X. Wei, J. Feng, K. Liu, Y. Dang, A. Zhou, Efficient and stable photoelectrochemical seawater splitting with TiO_2@g-C_3N_4 nanorod arrays decorated by Co-Pi, J. Phys. Chem. C 115 (2015) 20283-20292.

[23] T. Giannakopoulou, I. Papailias, N. Todorova, N. Boukos, Y. Liu, J. Yu, C. Trapalis, Tailoring the energy band gap and edges' potentials of g-C_3N_4/TiO_2

composite photocatalysts for NO_x removal, Chem. Eng. J. 310 (2017) 571-580.

[24] J. Wang, W. Zhang, Modification of TiO_2 nanorod arrays by graphite-like C_3N_4 with high visible light photoelectrochemical activity, Electrochim. Acta 71 (2012) 10-16.

[25] Y. Bu, Z. Chen, Effect of oxygen-doped C_3N_4 on the separation capability of the photoinduced electron-hole pairs generated by O-C_3N_4@TiO_2 with quasi-shell-core nanostructure, Electrochim. Acta 144 (2014) 42-49.

[26] C. Pan, J. Xu, Y. Wang, D. Li, Y. Zhu, Dramatic activity of C_3N_4/$BiPO_4$ photocatalyst with core/shell structure formed by self-assembly, Adv. Funct. Mater. 22 (2012) 1518-1524.

[27] W. Ma, D. Han, M. Zhou, H. Sun, L. Wang, X. Dong, L. Niu, Ultrathin g-C_3N_4/TiO_2 composites as photoelectrochemical elements for the real-time evaluation of global antioxidant capacity, Chem. Sci. 5 (2014) 3946-3951.

[28] S. Guo, Z. Deng, M. Li, B. Jiang, C. Tian, Q. Pan, H. Fu, Phosphorus-doped carbon nitride tubes with a layered micro-nanostructure for enhanced visible-light photocatalytic hydrogen evolution, Angew. Chem. Int. Ed. 55 (2016) 1830-1834.

[29] J. Su, P. Geng, X. Li, Q. Zhao, X. Quan, G. Chen, Novel phosphorus doped carbon nitride modified TiO_2 nanotube arrays with improved photoelectrochemical performance, Nanoscale 7 (2015) 16282-16289.

[30] S. Lin, X. Ye, X. Gao, J. Huang, Mechanistic insight into the water photooxidation on pure and sulfur-doped g-C_3N_4 photocatalysts from DFT

calculations with dispersion corrections, J. Mol. Catal. A-Chem. 406 (2015) 137-144.

[31] G. Zhang, M. Zhang, X. Ye, X. Qiu, S. Lin, X. Wang, Iodine modified carbon nitride semiconductors as visible light photocatalysts for hydrogen evolution, Adv. Mater. 26 (2014) 805-809.

[32] Y. Yan, Z. Li, Z. Zou, Photodegradation of rhodamine B and methyl orange over boron-doped g-C_3N_4 under visible light irradiation, Langmuir 26 (2010) 3894-3901.

[33] Q. Ruan, W. Luo, J. Xie, Y. Wang, X. Liu, Z. Bai, C. Carmalt, J. Tang, A nanojunction polymer photoelectrode for efficient charge transport and separation, Angew. Chem. Int. Ed. 56 (2017) 8221-8225.

[34] G. Govindaraju, G. Wheeler, D. Lee, K. Choi, Methods for electrochemical synthesis and photoelectrochemical characterization for photoelectrodes, Chem. Mater. 29 (2017) 355-370.

[35] S. Zhao, J. Liu, C. Li, W. Ji, M. Yang, H. Huang, Y. Liu, Z. Kang, Tunable ternary (N, P, B)-doped porous nanocarbons and their catalytic properties for oxygen reduction reaction, ACS Appl. Mater. Interfaces 6 (2014) 22297-22304.

[36] F. Boccuzzi, A. Chiorino, M. Manzoli, D. Andreeva, T. Tabakova, FT-IR study of the low-temperature water-gas shift reaction on Au/Fe_2O_3 and Au/TiO_2 catalysts, J. Catal. 188 (1999) 176-185.

[37] M. Kawaguchi, T. Kawashima, T. Nakajima, Syntheses and structures of new graphite-like materials of composition BCN(H) and BC_3N(H), Chem. Mater. 8

(1996) 1197-1201.

[38] L. Song, L. Ci, H. Lu, P. Sorokin, C. Jin, J. Ni, A. Kvashnin, D. Kvashnin, J. Lou, B. Yakobson, P. Ajayan, Large scale growth and characterization of atomic hexagonal boron nitride layers, Nano Lett. 10 (2010) 3209-3215.

[39] X. Pan, M. Yang, X. Fu, Z. Zhang, X. Xu, Defective TiO_2 with oxygen vacancies: synthesis, properties and photocatalytic applications, Nanoscale 5 (2013) 3601-3614.

[40] Y. Wang, Y. Shao, D. Matson, J. Li, Y. Lin, Nitrogen-doped graphene and its application in electrochemical biosensing, ACS Nano 4 (2010) 1790-1798.

[41] E. Hosono, S. Fujihara, H. Imai, I. Honma, I. Masaki, H. Zhou, One-step synthesis of nano-micro chestnut TiO_2 with rutile nanopins on the microanatase octahedron, ACS Nano 1 (2007) 273-278.

[42] I. Cho, Z. Chen, A. Forman, D. Kinm, P. Rao, T. Jaramillo, X. Zhen, Branched TiO_2 nanorods for photoelectrochemical hydrogen production, Nano Lett. 11 (2011) 4978-4984.

[43] G. Li, E. Sproviero, W. McNamara, R. Snoeberger, R. Crabtree, G. Brudvig, V. Batista, Reversible visible-light photooxidation of an oxomanganese water-oxidation catalyst covalently anchored to TiO_2 nanoparticles, J. Phys. Chem. B 114 (2010) 14214-14222.

[44] K. Schwinghammer, M. Mesch, V. Duppel, C. Ziegler, J. Senker, B. Lotsch, Crystalline carbon nitride nanosheets for improved visible-light hydrogen evolution, J. Am. Chem. Soc. 136 (2014) 1730-1733.

[45] J. Gunjakar, T. Kim, H. Kim, I. Kim, S. Hwang, Mesoporous layer-by-layer ordered nanohybrids of layered double hydroxide and layered metal oxide: highly active visible light photocatalysts with improved chemical stability, J. Am. Chem. Soc. 133 (2011) 14998-15007.

[46] D. Zhang, C. Pang, X. Wang, The function-led design of Z-scheme photocatalytic systems based on hollow carbon nitride semiconductors, Chem. Commun. 51 (2015) 17467-17470.

[47] Q. Yu, X. Meng, T. Wang, P. Li, J. Ye, Hematite films decorated with nanostructured ferric oxyhydroxide as photoanodes for efficient and stable photoelectrochemical water splitting, Adv. Funct. Mater. 25 (2015) 2686-2692.

[48] F. Abdi, L. Han, A. Smets, M. Zeman, B. Dam, R. Krol, Efficient solar water splitting by enhanced charge separation in a bismuth vanadate-silicon tandem photoelectrode, Nat. Commun. 4 (2013) 2195.

[49] J. Seabold, K. Choi, Efficient and stable photo-oxidation of water by a bismuth vanadate photoanode coupled with an iron oxyhydroxide oxygen evolution catalyst, J. Am. Chem. Soc. 134 (2012) 2186-2192.

[50] T. Kim, K. Choi, Nanoporous $BiVO_4$ photoanodes with dual-layer oxygen evolution catalysts for solar water splitting, Science 343 (2014) 990-994.

[51] G. Liu, W. Jaegermann, J. He, V. Sundström, L, Sun, XPS and UPS Characterization of the TiO_2/ZnPcGly heterointerface: alignment of energy levels, J. Phys. Chem. B 106 (2002) 5814-5819.

[52] X. Zhang, B. Zhang, K. Cao, J. Brillet, J. Chen, M. Wang, S. Yan, A perovskite

solar cell-TiO_2@$BiVO_4$ photoelectrochemical system for direct solar water splitting, J. Mater. Chem. A 3 (2015) 21630-21636.

[53] M. Gui, W. Zhang, Q. Su, C. Chen, Preparation and visible light photocatalytic activity of Bi_2O_3/Bi_2WO_6 heterojunction photocatalysts, J. Solid State Chem. 184 (2011) 1977-1982.

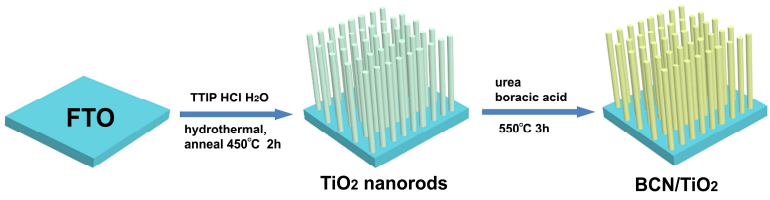

Fig. 1 Schematic diagram of the BCN/TiO_2 photoanode.

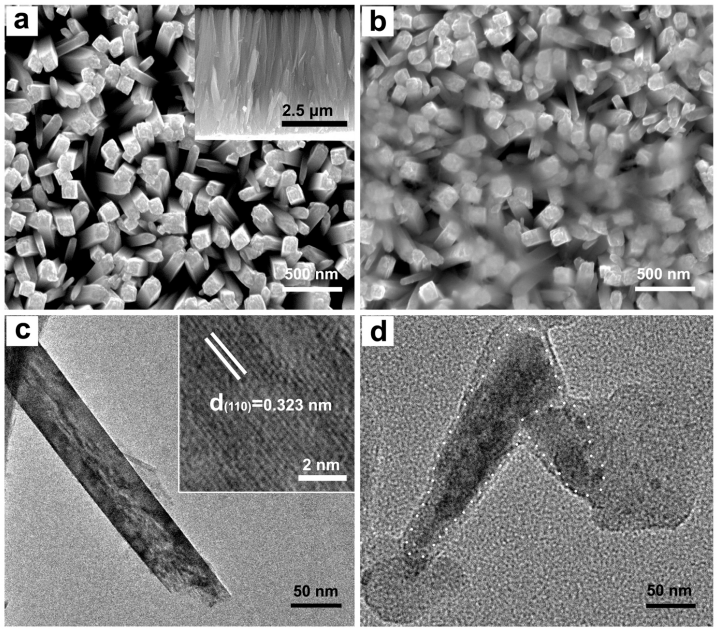

Fig. 2 SEM images of the TiO_2 (a) and BCN/TiO_2 (b). TEM images of the TiO_2 (c) and BCN/TiO_2 (d).

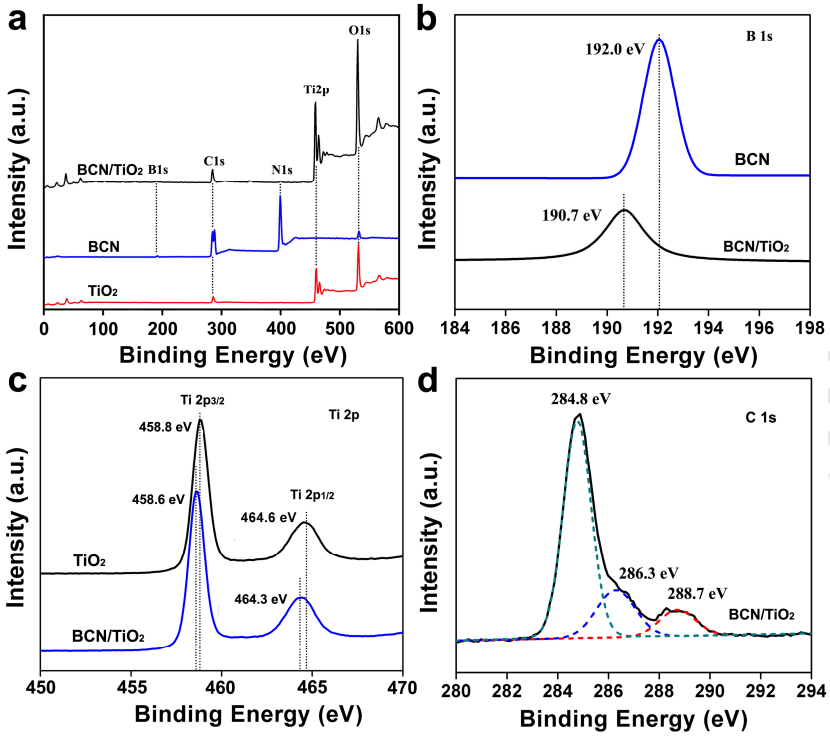

Fig. 3 (a) The full XPS spectra of the TiO_2, BCN and BCN/TiO_2. The high-resolution XPS spectra of B 1s (b), Ti 2p (c) and C 1s (d).

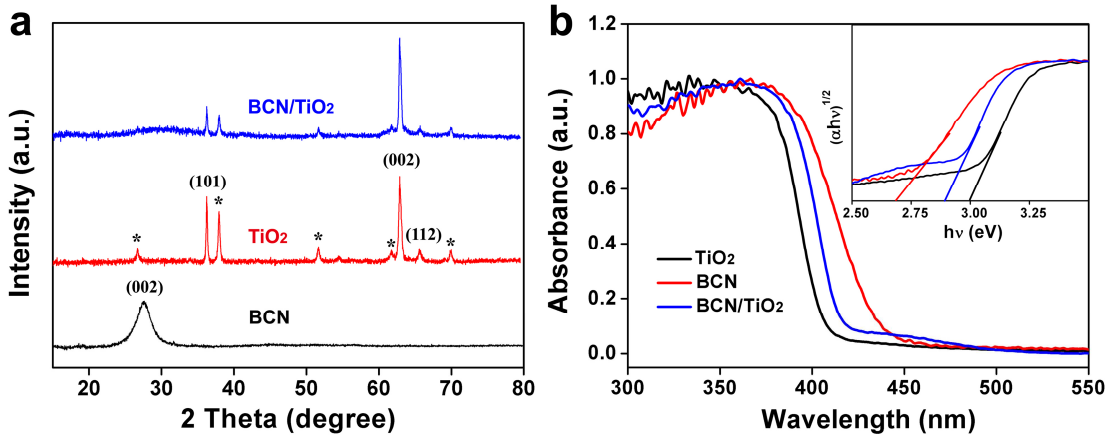

Fig. 4 XRD patterns (a) and the normalized UV-vis spectra (b) of the TiO_2, BCN and BCN/TiO_2 (Inset of Fig. 2b is the corresponding Tauc plots).

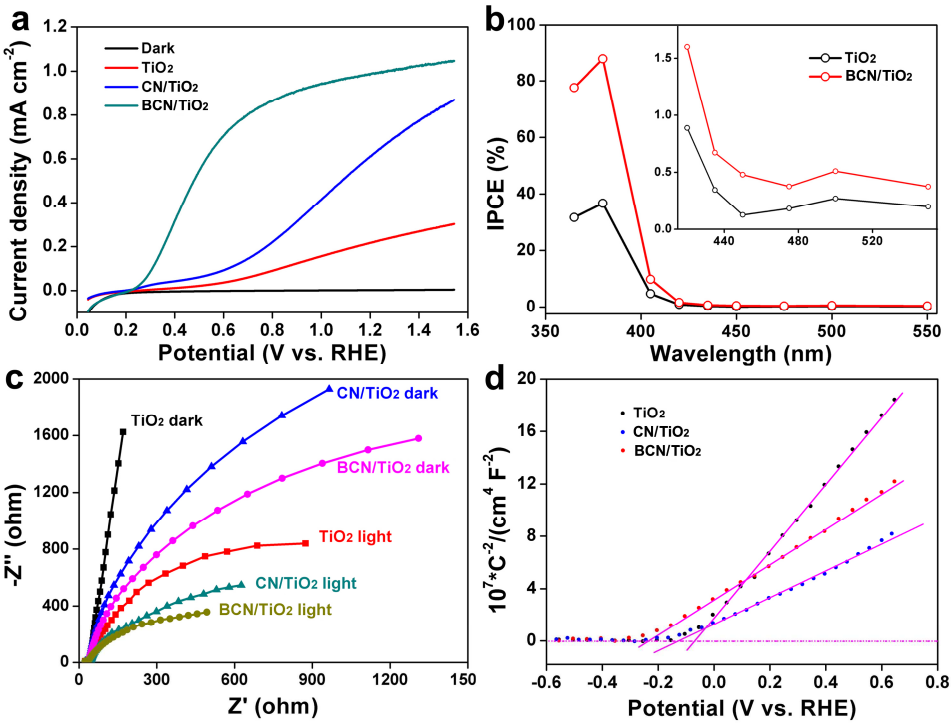

Fig. 5 (a) LSV curves of TiO_2 and BCN/TiO_2 with a scan rate of 10 mV/s under light illumination (100 mW cm^{-2}, AM 1.5 G). (b) IPCE plots of TiO_2 and BCN/TiO_2 obtained at 1.23 V vs. RHE. The inset image is the magnification IPCE data within 400~550 nm. (c) Nyquist plots of the TiO_2, CN/TiO_2 and BCN/TiO_2 measured in dark and under illumination. (d) The Mott-Schottky plots of the TiO_2, CN/TiO_2 and BCN/TiO_2 collected at a frequency of 1 kHz in dark.

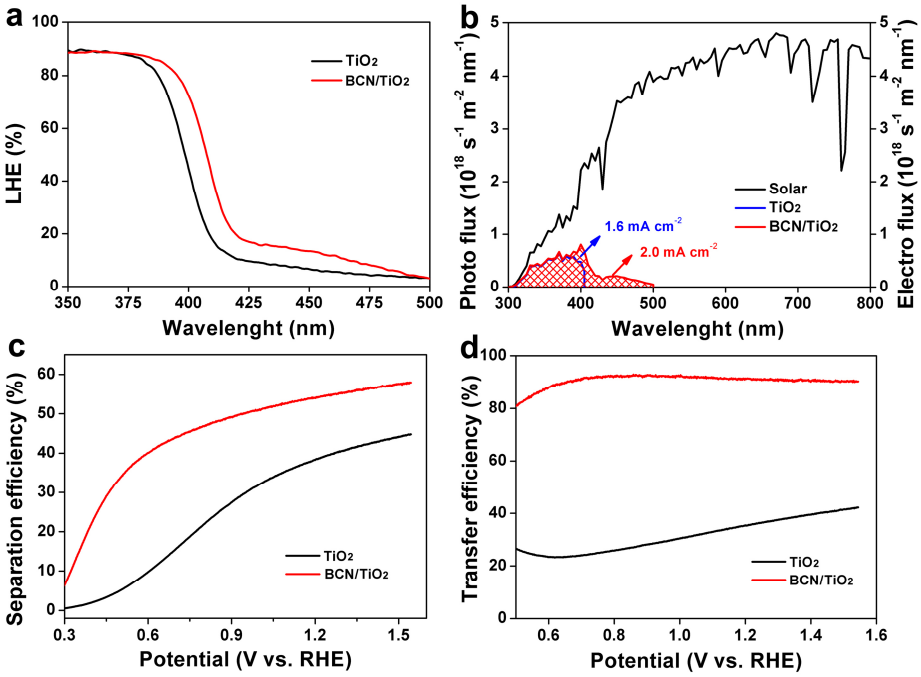

Fig. 6 Light harvesting efficiency (LHE) plots (a) and the AM 1.5 G photon flux incident at each wavelength and J_{abs} (b) of TiO_2 and BCN/TiO_2. The charge separation efficiency η_{sep} (c) and charge transfer efficiency $\eta_{transfer}$ (d) of TiO_2 and BCN/TiO_2.

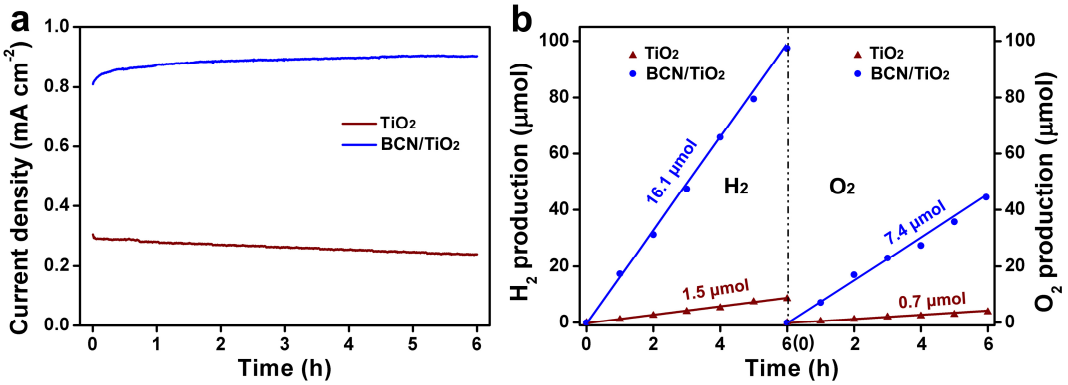

Fig. 7 (a) i-t curves of TiO_2 and BCN/TiO_2 photoanodes at 1.23 V vs. RHE. (b) Typical time course of H_2 and O_2 production from water for TiO_2 and

BCN/TiO_2 under light illumination (100 mW cm^{-2}, AM 1.5 G), in which the dots represent experimental data and the solid lines are the fitting curves.

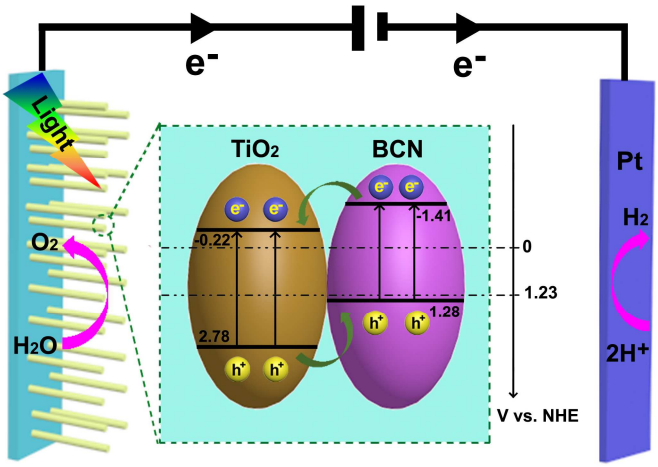

Fig. 8 Schematic illustration of the BCN/TiO_2 photoanode.

- BCN/TiO_2 hetero-junction is fabricated via in-situ thermal polymerization method.
- A 4-fold increase of the photocurrent density is obtained for BCN/TiO_2.
- The onset potential of BCN/TiO_2 exhibits a negative shift with 100 mV.
- Light absorption and charge separation/transfer process are improved for BCN/TiO_2.